A precise deuterium abundance: remeasurement of the $z = 3.572$ absorption system towards the quasar PKS1937–101

S. Riemer-Sørensen,[1,2]★ S. Kotuš,[3]★ J. K. Webb,[4] K. Ali,[5] V. Dumont,[4,6]
M. T. Murphy[3] and R. F. Carswell[7]

[1]*Institute of Theoretical Astrophysics, The University of Oslo, Boks 1072 Blindern, NO-0316 Oslo, Norway*
[2]*ARC Centre of Excellence for All-sky Astrophysics (CAASTRO), Institute of Theoretical Astrophysics, The University of Oslo, Boks 1072 Blindern, NO-0316 Oslo, Norway*
[3]*Centre for Astrophysics and Supercomputing, Swinburne University of Technology, PO Box 218, Hawthorn VIC 3122, Australia*
[4]*School of Physics, University of New South Wales, Sydney NSW 2052, Australia*
[5]*International Centre for Radio Astronomy Research (ICRAR), University of Western Australia, 35 Stirling Hwy, Crawley WA 6009, Australia*
[6]*Department of Physics, University of California, Berkeley, CA 94720-7300, USA*
[7]*Institute of Astronomy, University of Cambridge, Madingley Road, Cambridge CB3 0HA, UK*

ABSTRACT

The primordial deuterium abundance probes fundamental physics during the big bang nucleosynthesis and can be used to infer cosmological parameters. Observationally, the abundance can be measured using absorbing clouds along the lines of sight to distant quasars. Observations of the quasar PKS1937–101 contain two absorbers for which the deuterium abundance has previously been determined. Here, we focus on the higher redshift one at $z_{abs} = 3.572$. We present new observations with significantly increased signal-to-noise ratio that enable a far more precise and robust measurement of the deuterium to hydrogen column density ratio, resulting in $D\,\textsc{i}/H\,\textsc{i} = 2.62 \pm 0.05 \times 10^{-5}$. This particular measurement is of interest because it is amongst the most precise assessments to date and it has been derived from the second lowest column-density absorber [$N(\mathrm{H\,\textsc{i}}) = 17.9\,\mathrm{cm}^{-2}$] that has so-far been utilized for deuterium abundance measurements. The majority of existing high-precision measurements were obtained from considerably higher column density systems [i.e. $N(\mathrm{H\,\textsc{i}}) > 19.4\,\mathrm{cm}^{-2}$]. This bodes well for future observations as low column density systems are more common.

Key words: nuclear reactions, nucleosynthesis, abundances – quasars: absorption lines – cosmological parameters – primordial nucleosynthesis.

1 INTRODUCTION

Any presence of non-standard physics, e.g. from dark matter or additional neutrinos, during the epoch of big bang nucleosynthesis (BBN) may change the conditions under which the light elements such as deuterium, helium and lithium formed and their resulting abundances (e.g. Steigman 2012; Bœhm, Dolan & McCabe 2013; Nollett & Steigman 2014; Archidiacono et al. 2015). While the observed abundances (apart from lithium) are in overall agreement with the standard model predictions, we need high-precision measurements (Izotov, Thuan & Guseva 2014; Aver, Olive & Skillman 2015) to distinguish between more detailed scenarios (e.g. Di Valentino, Melchiorri & Mena 2013; Steigman 2013).

The abundance of deuterium traces the number density of baryons at early times, which can also be determined from the cosmic microwave background (CMB; Fixsen 2009). *Planck* provides the highly precise measurement of $\Omega_b h^2 = 0.022\,25 \pm 0.000\,16$ (where

h is the dimensionless Hubble parameter $H_0 = 100h\,\mathrm{km\,s^{-1}\,Mpc^{-1}}$) at the time of recombination (Planck Collaboration III 2016), which can be compared to the value obtained from BBN to infer any time evolution.

In this paper, we present a new and precise measurement of the deuterium abundance in the absorption system at $z_{abs} = 3.572$ towards the quasar PKS1937–101 (B1950, emission redshift $z_{em} = 3.787$; Lanzetta et al. 1991). The deuterium abundance has previously been determined in two well-separated absorption systems in the sight-line to PKS1937–101 at $z_{abs} = 3.256$ (Crighton et al. 2004) and $z_{abs} = 3.572$ (Tytler, Fan & Burles 1996; Burles & Tytler 1998a). Here, we focus on the $z_{abs} = 3.572$ absorber, previously suggested as an ideal absorber for a $D\,\textsc{i}/H\,\textsc{i}$ measurement, due to its low metallicity, high column density and simple velocity structure (Tytler et al. 1996). The low-redshift system was re-analysed in a companion paper (Riemer-Sørensen et al. 2015). Since the first measurements were published, PKS1937–101 has been the target of extensive observations with both the Ultraviolet and Visual Echelle Spectrograph (UVES) at the Very Large Telescope (VLT) and the High Resolution Echelle Spectrometer (HIRES) at the Keck

Table 1. Observations included in the analysis (including those of table 1 in Riemer-Sørensen et al. 2015).

Date	Primary investigator	Instrument	Settings[a]	Resolving power	Resolution[b] σ_v(km s^{-1})	Observation time (ks)
1996-08-09	Songaila	Keck LRIS	$w = 0.7$ arcsec and 1.5 arcsec	1500, 300	400	2.4, 2.7
1997-10-02	Cowie	Keck HIRES	C5 (1.148 arcsec, 4000/6480 Å)	37 000	3.5	4×2.4
1997-10-03	Cowie	Keck HIRES	C5 (1.148 arcsec, 3910/6360 Å)	37 000	3.5	4×2.4
1997-10-04	Cowie	Keck HIRES	C5 (1.148 arcsec, 3910/6360 Å)	37 000	3.5	$2 \times 2.4 + 1 \times 1.4$
2005-07-01	Crighton	Keck HIRES	B5 (0.861 arcsec, 3630/8090 Å)	49 000	2.8	6×3.6
2005-08-12	Tytler	Keck HIRES	C5 (1.148 arcsec, 3790/6730 Å)	37 000	3.5	$2 \times 6.4 + 1 \times 6.0$
2006-04-10	Carswell[c]	VLT UVES	DICHR#1 (1.0 arcsec, 3900/5800 Å)	45 000	2.8	1×5.4
2006-06-01	Carswell[c]	VLT UVES	DICHR#1 (1.0 arcsec, 3900/5800 Å)	45 000	2.8	2×5.4
2006-06-25	Carswell[c]	VLT UVES	DICHR#1 (1.0 arcsec, 3900/5800 Å)	45 000	2.8	1×5.4
2006-07-21	Carswell[c]	VLT UVES	DICHR#1 (1.0 arcsec, 3900/5800 Å)	45 000	2.8	1×5.4

Notes. [a]Slit width for LRIS, slit width, cross-disperser angle and central wavelength for HIRES, and slit width and central wavelength of the blue/red arms for UVES.
[b]1σ velocity width of the resolution element, σ_v, as determined by illuminating the instrument with a Thorium–Argon lamp. The individual σ_v have been χ^2 optimized as described in Section 3.3.
[c]All VLT UVES observations belong to the ESO programme with ID 077.A-0166(A).

Telescope, so that the total exposure time has increased by almost a factor of 10.

The precision of the measurement presented here is similar to those of Cooke et al. (2014), but from a much lower column density absorber with $N(\text{H \textsc{i}}) = 17.9\,\text{cm}^{-2}$ versus $N(\text{H \textsc{i}}) > 19.4\,\text{cm}^{-2}$.

In Section 2, we present the observational data, and the analysis details in Section 3. The results are presented in Section 3.6 with the details of the best-fitting model given in Appendix A. In Section 4, we discuss various caveats such as the probability of blending, and compare the new measurements to those from previous studies and also to the estimate of $\Omega_b h^2$ from the *Planck* measurement of the CMB. We also investigate any cosmological implications before concluding in Section 5.

Unless otherwise stated, we quote uncertainties as 68 per cent confidence level, and column densities are quoted as $\log(N)$ where N has the unit of cm^{-2}.

2 OBSERVATIONS

The observational data used in this paper are listed in Table 1. It includes all the observations listed in table 1 of Riemer-Sørensen et al. (2015) plus an additional publicly available Keck observation.[1] The observations are reduced and continuum-fitted using standard procedures as described in Riemer-Sørensen et al. (2015). In Section 3.2, we discuss possible continuum-level uncertainties and how we account for them.

The individual quasar exposures taken with similar grating settings and slit-widths (i.e. resolving powers) were combined with inverse-variance weighting. This provided a total of five final spectra that, if combined, would completely cover the wavelength range of 4100–6400 Å. The average signal-to-noise ratio of the fitted Lyman regions varies from 14 to 65 for pixel sizes of 2.5–4.3 km s^{-1} (the individual values are given in Table 2).

3 ANALYSIS AND RESULTS

A more complete description of the analysis methods is given in Riemer-Sørensen et al. (2015). Here, we provide additional details specific to the analysis described in this paper.

[1] Keck Observatory Archive; http://www2.keck.hawaii.edu/koa/public/koa.php.

Table 2. Signal-to-noise ratios (S/N) of the fitted Lyman series regions.

Transition	Width (km s^{-1})	HIRES (S/N)	Pixel size (km s^{-1})	UVES (S/N)	Pixel size (km s^{-1})
Lyman α	1104	60	3.2	46	2.5
Lyman β	563	65	3.9	–	–
Lyman γ	539	36	4.1	21	2.5
Lyman 4	450	23	4.1	14	2.5
Lyman 5	406	36	4.2	27	2.5
Lyman 6	366	36	4.2	26	2.5
Lyman 7	391	28	4.3	23	2.5
Lyman 8	614	40	4.3	28	2.5
Lyman 9	278	29	4.3	21	2.5

3.1 Spectral fitting

The five individual spectra (Section 2) are fitted simultaneously but separately, rather than being combined into a single, composite spectrum as is more commonly the approach. For visualization we use a variance-weighted stacked spectrum of the HIRES and UVES spectra as shown in Fig. 1. We fit six heavy element transitions: Fe III 1122, Si II 1193, Si II 1304, Si IV 1393, Si IV 1402 and C II 1334, and nine Lyman transitions (from Lyman α to Lyman 9) together with the saturated Lyman limit in the lower resolution spectrum from the Low Resolution Imaging Spectrometer (LRIS) at the Keck Telescope. We include the LRIS Lyman limit data to better constrain the hydrogen column density.

To optimize the accuracy of our measurement, we solve for the total column density in the absorption complex rather than the column densities of the individual subcomponents. We force the column density ratio of D I/H I to be identical across all subcomponents, which corresponds to assuming that any deuterium depletion mechanisms act uniformly on all components. This is a reasonable assumption as the total metallicity of the absorber is less than 1/100th of the solar value (Section 3.7). The column densities of the other species are allowed to vary between components.

To assess whether the scatter in current deuterium measurements (see Table 4 and Fig. 4) might be correlated with the observing telescopes, we also fitted the model to the spectra from Keck alone and from VLT alone, in addition to the entire data set.
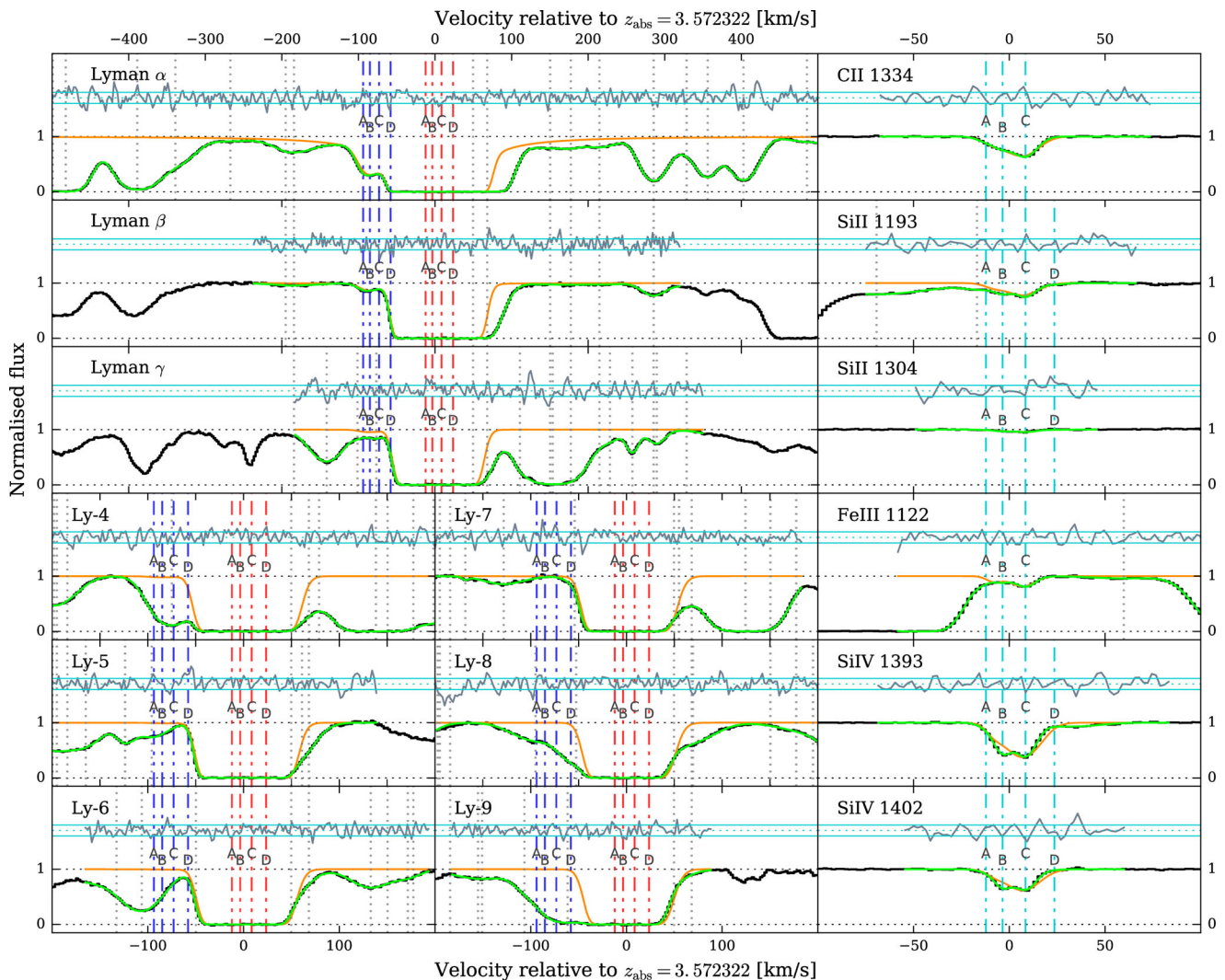
Figure 1. The composite spectrum, created by combining the four different exposure stacks used in the analysis with variance weighting (thick black), the final model fit (thick green/light grey) and the residuals between the two (grey, above the spectrum in each panel) normalized by the 1σ error array (indicated by light blue horizontal lines). This composite spectrum is not used in the analysis; it is for visualization purposes only and the analysis uses the four exposure stacks simultaneously to constrain the model fit parameters. The vertical dot–dashed lines mark the velocity components A–D: red/light grey for H I, blue/dark grey for D I, light blue/light grey for heavy elements. Interloping H I absorption is marked by light grey vertical dotted lines. The model from Tytler et al. (1996) (without blends) is overplotted (thin orange/grey). It is clear that we find a different structure particularly for the metals.

3.2 Velocity shifts and continuum

As in Riemer-Sørensen et al. (2015), we explicitly allow for small velocity shifts between individual exposures that are expected to arise from slit-centring and wavelength calibration differences. We effectively force all regions from a given spectrum to have identical shifts. The only exception is the VLT spectrum of the Lyman 5 region where the preferred velocity shift ($\approx 1.1\,\mathrm{km\,s^{-1}}$) differs to the other regions in the same spectrum ($\approx 0.5\,\mathrm{km\,s^{-1}}$) and we have introduced that shift as an extra free parameter during the χ^2 minimization process. Allowing independent shifts in any of the other regions did not improve the χ^2 per degree of freedom (χ^2/dof).

To account for possible uncertainties in the continuum level determination, we fit a local continuum in each region. Where a reasonable amount of unabsorbed continuum is available on both sides of the line, we allow for a local slope on the continuum (C II 1334 and Lyman β, 5, 7, 8), but otherwise we keep the slope fixed at zero (Fe III, Si II, Si IV and Lyman α, γ, 4, 6, 9).

Both the continua and the best-fitting velocity shifts are given in Table A1, and we apply them before combining the spectra for visualization as shown in Fig. 1.

3.3 Spectral resolution

The spectral resolution in velocity units, σ_v, is given in the telescope manuals[2] based on exposures with a Thorium–Argon lamp. For science exposures of the quasar, the slit may not be uniformly filled, unlike for the Thorium–Argon exposures. This may lead to a difference between the Thorium–Argon line width and the actual spectral resolution. We explored this possibility by varying the spectral resolution of each individual fitting region so as to minimize the overall χ^2 for the fit while keeping all other parameter

Table 3. Best-fitting parameters of the models described in Section 3.4.

Spectra	χ^2/dof	$\log(N(\mathrm{D\,I}))$	$\log(N(\mathrm{H\,I}))$	$\log(N(\mathrm{D})/N(\mathrm{H}))$	D I/H I [$\times 10^{-5}$]
All	1.04	13.344 ± 0.0056	17.925 ± 0.0063	-4.581 ± 0.008	2.62 ± 0.051
Keck+LRIS	1.00	13.357 ± 0.0244	17.925 ± 0.0066	-4.568 ± 0.025	2.70 ± 0.157
VLT+LRIS	1.12	13.332 ± 0.0287	17.921 ± 0.0068	-4.589 ± 0.030	2.58 ± 0.175

Note that we present additional significant figures for the parameter estimates in this table only to allow reproduction of our final uncertainty estimates in the D I/H I in the final column.
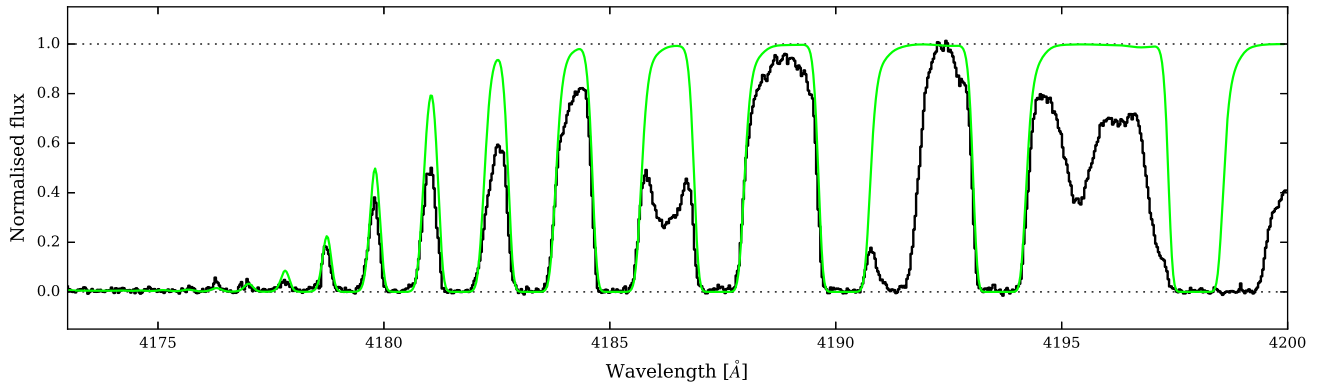

Figure 2. The stacked high-resolution spectra (weighted by inverse variance) of the Lyman limit (thick black) with the best-fitting model (thin green/grey) based on the first nine Lyman transitions. It is clear that the model and the limit are consistent, but many blends are needed to fully model the limit and the continuum is not well defined.

values fixed. Of the 72 individually fitted regions, the resolution was changed from the Thorium–Argon estimate for 14, of which only three required more than a 20 per cent adjustment. After this optimization, the resolutions were kept fixed during the fit. Re-running the fit after the adjustments of the resolution improved the total χ^2/dof by ~ 0.15.

3.4 Models

The absorption signature just bluewards of the strongest hydrogen lines (Lyman α, β and γ) is visible in the composite spectrum in Fig. 1. Its velocity is offset by $-88 \pm 13\,\mathrm{km\,s^{-1}}$ from the main absorption, consistent with the expected deuterium–hydrogen separation of $82\,\mathrm{km\,s^{-1}}$. Further, this absorption line is significantly narrower than other nearby Lyman lines, but significantly broader than is typical for heavy element absorption lines. We thus interpret this line as being due to D I (see also Section 4.1).

The composite spectrum in Fig. 1 shows that the Si IV absorption comprises at least two velocity components, which are both slightly asymmetric. We model this with four Voigt profiles (velocity components A, B, C, D) that we require to have identical redshifts, temperatures and turbulent b-parameters across all species, but individual summed column densities. Only the column density ratio of D I to H I is assumed to be the same for components A–D, the remaining relative abundances are free to vary. The B and C components are clearly visible in all heavy elements, while A and D have lower column densities and D is not required to adequately fit the weaker metal transitions of C II and Fe III for which the column densities drop below the threshold value of $\log(N) < 8$ and are removed from the fit.

Adding additional components to the system did not improve the χ^2/dof significantly. To avoid biasing, the final model for the absorption system was selected based on χ^2/dof without checking the impact on the D/H ratio.

The presence of multiple heavy element species makes it possible to simultaneously fit for both temperature and b-parameters for the main components (A–D).

The best-fitting χ^2/dof is 1.04 with the resulting parameters given in Table A1 and the H I and D I column densities given in Table 3.

The species of C II, Si II, Fe III and H I have significantly lower ionization potentials than Si IV, which therefore may not always trace the full velocity structure of the lower ionization species (Wolfe & Prochaska 2000; Fox et al. 2007). In locations where we find Si IV there is also bound to be hydrogen, but it may not be in the form of H I. In the model fitting, this is taken into account by keeping the column densities of the individual species unrelated. If the fit is good (based on χ^2/dof) without H I for a given component in Si IV VPFIT will automatically remove the component. Consequently, the probability of finding the correct velocity structure is higher when we use the entire range of metals available, and including the higher ionization species should not bias D I/H I. We note that all components present in Si IV are also present in Si II, but with the velocity structure much better resolved in Si IV. Refitting without Si IV leads to a simpler velocity structure with only two components, but also a significant increase in χ^2/dof, e.g. 1.19–1.59, for the C II regions. We conclude from this that Si IV helps significantly in determining the velocity structure.

O I is not clearly present in the individual spectra, but when fitting all spectra simultaneously, we obtain a non-zero summed column density based on O I 1302 under the assumption of constant O I/H I across all components (see Table A1). The O I column density is used as input for CLOUDY simulations in Section 3.7 to determine the metallicity of the absorber.

3.5 Fitting the Lyman limit

The high-resolution spectra of the Lyman limit contain many blended Lyman series lines that makes it harder to establish a reliable continuum level and complicates the modelling. Instead, we
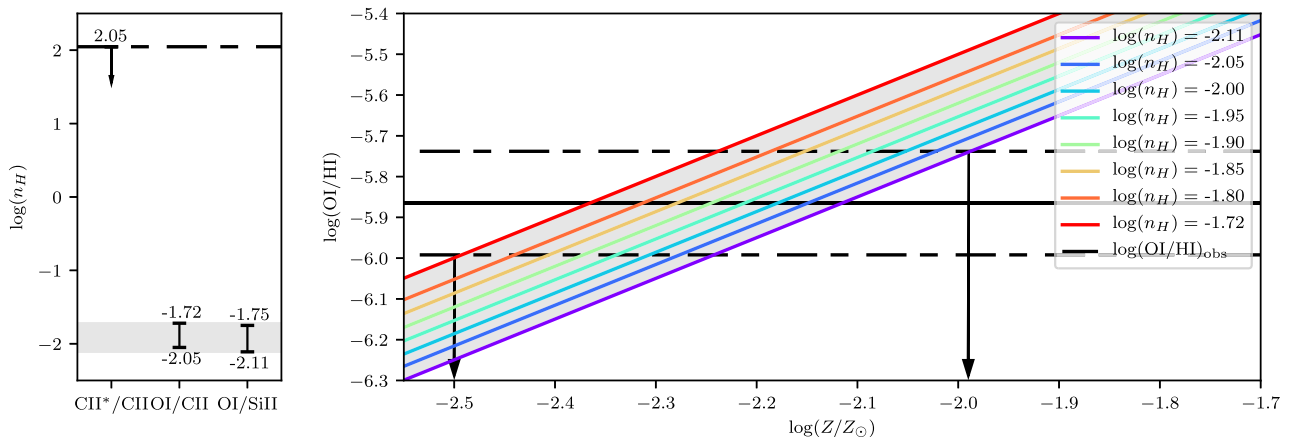
Figure 3. Left: the particle density range, $\log(n_H)$, inferred using CLOUDY photoionization models based on the column density ratios derived from the quasar spectra using VPFIT. The upper limit from C II*/C II = 0.16 assumes fully neutral hydrogen (equation 61 in Bahcall & Wolfe 1968). In practice, partial ionization is possible, which will decrease the actual upper limit, in agreement with the values obtained from O I/C II and O I/Si II. The grey shaded area indicate the limits on $\log(n_H)$ used in the subsequent analysis. Right: O I/H I column density ratio as a function of metallicity for increasing particle densities (from top to bottom). The observationally derived O I/H I column density is given by the horizontal line and the dashed lines span the uncertainty. The arrows indicate the extreme metallicities that are compatible with the allowed range of $\log(n_H)$ for the observed column density.

verify that the model derived using the first nine lines in the Lyman series is consistent with the observed Lyman limit data as shown in Fig. 2.

3.6 Resulting deuterium and hydrogen column densities

Table 3 gives the resulting column densities of D I and H I and the ratios derived using the different data subsets. The main result from combining these measurements is a D I/H I column density ratio of $2.62 \pm 0.05 \times 10^{-5}$.

The spectra from the two different telescopes separately provide consistent results within the 1σ uncertainties, with the Keck spectrum leading to a slightly higher estimate of the D I/H I ratio: $(D I/H I)_{Keck} = 2.70 \pm 0.16 \times 10^{-5}$ compared to $(D I/H I)_{VLT} = 2.58 \pm 0.18 \times 10^{-5}$. This difference is much less than the combined uncertainties involved and there is no evidence to suspect any systematic deviation between the two telescopes.

The uncertainties quoted above and in Table 3 are only statistical; they derive from the signal-to-noise ratio of the spectra and do not include any systematic error estimates. However, the larger values of χ^2/dof for the alternative models in Section 3.4, and the agreement between the results from different data sets, both suggest that the overall measurement is robust.

3.7 Metallicity

Following the method from Riemer-Sørensen et al. (2015), we use CLOUDY simulations to determine the hydrogen number density and the metallicity of the main absorbers (Ferland et al. 2013). In the CLOUDY modelling, we used a plane parallel geometry and a Haardt–Madau HM05 model[3] as the ultraviolet background source. We generate a grid of models with the hydrogen number density bounded by $-5 < \log(n_H[\text{cm}^{-3}]) < 2.04$, where the high-density limit comes from the upper limit to C II*/C II ratio determined as in Riemer-Sørensen et al. (2015).

---

[3] Described in section 6.11.8 of the CLOUDY documentation, http://www.nublado.org/browser/ branches/c13_branch/docs/hazy1_c13.pdf.

The O I/H I and Si II/H I ratios are fairly insensitive to n_H and provide an allowable range of metallicity of $-3 \lesssim \log(Z/Z_\odot) \lesssim -1$ given the observational data. The left-hand panel of Fig. 3 shows the $\log n_H$ range obtained by comparing CLOUDY models with the observed abundances. The lower ionization species agree with one another, leading to a conservative number density constraint $-2.11 < \log(n_H) < -1.72$.

From the Voigt profile fit, we obtain a marginal detection of O I with a summed column density of $\log N(\text{O i}) = 12.060 \pm 0.127$. The O I/H I ratio is sensitive to the metallicity Z within the given n_H range as shown in the right part of Fig. 3 (arrows) and provides a constraint of $-2.50 < \log(Z/Z_\odot) < -1.99$. The simplest of chemical evolution models, as investigated by Fields et al. (2001), indicates little to no depletion of primordial deuterium for $\log(Z/Z_\odot) < -1$; hence, this system appears to be a good estimator of initial D I/H I, given the allowable metallicity range.

We check the consistency of the CLOUDY models by comparing the output gas temperature with that estimated by VPFIT. The CLOUDY models take into account the average properties of all four components and provide a temperature range of $T_{\text{CLOUDY}} = 14\,500 - 16\,300$ K. From VPFIT, the temperature is best determined for the dominating individual components A and C. The resulting temperatures of $T_{\text{VPFIT}}^{\text{A}} = 16\,410 \pm 370$ K and $T_{\text{VPFIT}}^{\text{C}} = 18\,650 \pm 658$ K, respectively, are based on absorption in all considered species. As can be seen, the temperature of models generated by CLOUDY is in reasonable agreement with that estimated by VPFIT.

Integrating through the absorbing cloud, i.e. allowing for varying particle density through the absorbing cloud, and taking into account the metallicity uncertainty, the cloud size is estimated as 2.7 ± 1.7 kpc.

4 DISCUSSION

4.1 Hydrogen contamination of deuterium lines

It is possible that the line identified as deuterium may be contaminated by a weak hydrogen line. Assuming the hydrogen column density distribution to be a power law with index $\beta = 1.7$

Table 4. The sample of D I/H I measurements considered robust in Pettini et al. (2008) together with updated estimates in the same absorbers and more recent, similarly precise measurements from other absorbers.

Reference	Absorption redshift	$\log(N(H\,\textsc{i}))$	[X/H]	D I/H I $(\times 10^{-5})$	$100\Omega_b h^2$
Burles & Tytler (1998a)	2.504	17.4 ± 0.07	-2.55 Si	4.00 ± 0.70	1.66 ± 0.18
Pettini & Bowen (2001)	2.076	20.4 ± 0.15	-2.23 Si	1.65 ± 0.35	2.82 ± 0.36
Kirkman et al. (2003)	2.426	19.7 ± 0.04	-2.79 O	2.43 ± 0.35	2.24 ± 0.20
Fumagalli et al. (2011)	3.411	18.0 ± 0.05	-4.20 Si	2.04 ± 0.61	2.49 ± 0.05
Noterdaeme et al. (2012)	2.621	20.5 ± 0.10	-1.99 O	2.80 ± 0.80	2.05 ± 0.35
Cooke et al. (2014), Pettini & Cooke (2012)	3.050	20.392 ± 0.003	-1.92 O	2.51 ± 0.05	2.19 ± 0.02
Cooke et al. (2014), O'Meara et al. (2001)	2.537	19.4 ± 0.01	-1.77 O	2.58 ± 0.15	2.16 ± 0.04
Cooke et al. (2014), Pettini et al. (2008)	2.618	20.3 ± 0.01	-2.40 O	2.53 ± 0.10	2.18 ± 0.03
Cooke et al. (2014)	3.067	20.5 ± 0.01	-2.33 O	2.58 ± 0.07	2.16 ± 0.03
Cooke et al. (2014), O'Meara et al. (2006)	2.702	20.7 ± 0.05	-1.55 O	2.40 ± 0.14	2.25 ± 0.03
Riemer-Sørensen et al. (2015)	3.255	18.1 ± 0.03	-1.87 O	2.45 ± 0.28	2.23 ± 0.16
Balashev et al. (2016)	2.437	19.98 ± 0.01	-2.04 O	1.97 ± 0.33	2.54 ± 0.26
This work	3.572	17.925 ± 0.006	-2.26 O	2.62 ± 0.05	2.14 ± 0.03
Weighted average[a]	–	–	–	2.55 ± 0.03	2.17 ± 0.03
Unweighted average[a]	–	–	–	2.53 ± 0.17	2.18 ± 0.08
Planck Collaboration III (2016)	–	–	–	2.45 ± 0.05	2.225 ± 0.016

Notes. The conversion between D I/H I and $\Omega_b h^2$ is based on nuclear rates from Coc et al. (2015) for standard BBNs.
[a]Without the Balashev et al. (2016) and Noterdaeme et al. (2012) measurements.

(Penton, Stocke & Shull 2004) and the redshift distribution to be a single power law with index $\gamma = 1.51 \pm 0.09$ and normalization $\log(A) = 0.72 \pm 0.08$ for $13.1 < N(H\,\textsc{i}) < 14.0$ (Kim et al. 2013), we can determine the probability of detecting a line within a given redshift and column density interval. We take the relevant redshift interval to be spanned by the 3σ edges of components A–D and D/H $= [10^{-5}, 10^{-4}]$, which for the determined hydrogen column density of $\log N(H\,\textsc{i}) = 17.925$ corresponds to $\log N(H\,\textsc{i}) = [12.925, 13.925]$ (H I and D I have the same oscillator strengths for the presumed Lyman α blending feature). This leads to a conservative estimate of the blending probability of 3.7 per cent. If we consider only the dominant component (A), the probability reduces to 0.25 per cent supporting the claim that the observed feature is likely to be deuterium.

We also checked whether any heavy element lines from other absorbers along the line of sight fall in the regions fitted to obtain D I/H I. We identified tentative systems with lines from commonly found heavy elements (Al, C, Fe, Mg, Si) at $z = [0.560\,30, 0.567\,90, 0.603\,12, 0.896\,83, 3.008\,51, 3.095\,45, 3.256\,18, 3.291\,34, 3.453\,59, 3.553\,57, 3.572\,30]$. The only potentially problematic blend is from Fe II 1144 at $z = 3.095$ that falls very close to D I in Lyman β. However, no other Fe II lines are present anywhere in the spectrum at this redshift, some of which have larger oscillator strengths than Fe II 1144. We therefore assume the Fe II 1144 at $z = 3.095$ is too weak to significantly bias the deuterium column density.

4.2 Comparison with previous measurements

Using an independent sample of Keck HIRES exposures, and only two velocity components to model the hydrogen absorption, Burles & Tytler (1998b) estimated the D I/H I ratio in the same absorber to be D I/H I $= 3.3 \pm 0.3 \times 10^{-5}$ without using the heavy element lines. The initial measurement presented in Tytler et al. (1996) was improved with an H I column density measurement of $\log(N(H\,\textsc{i})) = 17.86 \pm 0.02$ based on the HIRES spectra with additional low-resolution spectra from LRIS and the Kast spectrograph on the Shane 3 metre Telescope at the Lick Observatory (Burles & Tytler 1997, 1998b).

The discrepancies between our new measurement and that of Burles & Tytler (1998b) may be due to several factors such as continuum placement, number of components and assumptions about physical properties of the absorber.

The continuum placement has been discussed in the literature. Wampler (1996) suggested models with three to six times larger H I column densities, while Songaila, Wampler & Cowie (1997) obtained $\log(N(H\,\textsc{i})) < 17.7$ from the LRIS spectrum used in this analysis. Without supplementary high-resolution spectra, their continuum may have been poorly estimated. According to Burles & Tytler (1997), the unabsorbed continuum was underestimated in Songaila et al. (1997), but comparing with the high-resolution spectra, we find that it is more likely to be overestimated. However, as we treat the local continua as free parameters, the discrepancy with Burles & Tytler (1998b) more likely origins in the different numbers of fitted components. We have overplotted the initial model from Tytler et al. (1996) on the stacked spectrum in Fig. 1 (without additional hydrogen blends). Burles & Tytler (1998b) did not use any of the heavy element lines to derive D I/H I, and consequently their (χ^2-based) choice of two components relies purely on the Lyman lines and not all the accessible information. Instead, here we assume that Si IV traces the H I velocity structure despite the difference in ionization potentials. The assumption is based on visual similarities in the spectrum combined with a significant increase in χ^2/dof if fitting a two-component model without Si IV (e.g. 1.19–1.59 for the C II regions). Fitting a four-component model without Si IV leads to very small column densities for two components and significantly increased uncertainties (see also details in Section 3.4).

4.3 The deuterium sample

Table 4 provides an updated version of the deuterium sample given in table 4 of Riemer-Sørensen et al. (2015), comparing the new D I/H I measurement presented in this paper to the sample from Pettini et al. (2008) combined with recent measurements with similar precisions from Fumagalli, O'Meara & Prochaska (2011), Noterdaeme et al. (2012), Cooke et al. (2014), Riemer-Sørensen et al. (2015) and Balashev et al. (2016).
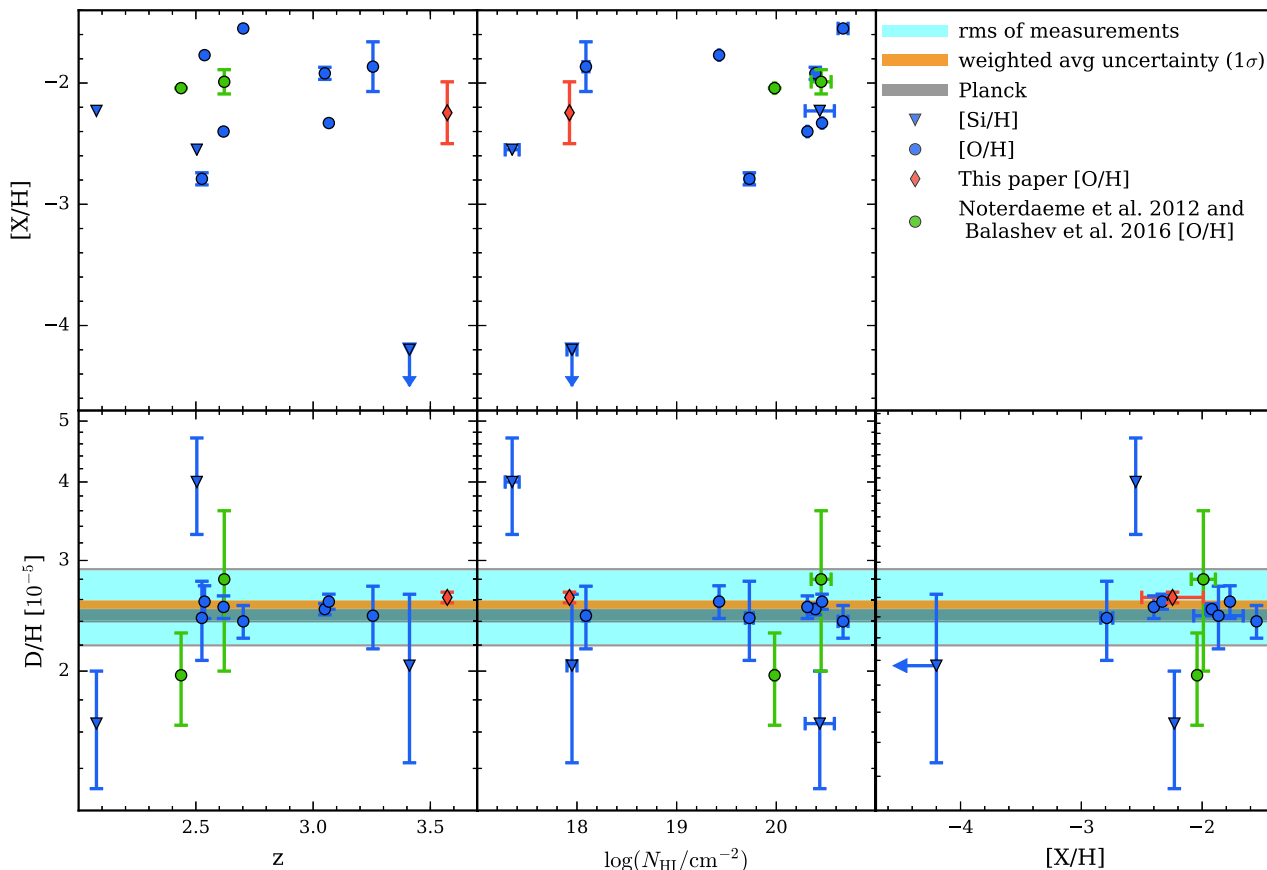
Figure 4. The D I/H I ratios and metallicities from the literature sample defined in Table 4 plotted as a function of redshift (z), H I column density ($\log(N(\text{H I}/\text{cm}^{-2}))$) and metallicity ([X/H]). The 1σ uncertainty in the weighted mean, D I/H I $=2.55 \pm 0.03 \times 10^{-5}$, is shaded orange while the outer cyan shading indicates the root-mean-square deviation amongst the measurements. The inner dark shading indicates the constraint on D I/H I derived from the *Planck* measurements assuming standard BBN.

Fig. 4 supersedes fig. 4 from Riemer-Sørensen et al. (2015), illustrating the properties of the absorption systems for the results given in Table 4. As in Riemer-Sørensen et al. (2015), we again find no apparent correlation between any of the parameters, including deuterium and hydrogen column density versus redshift or metallicity.

The measurement from Balashev et al. (2016) is derived from a fairly complicated absorption system under the assumption that the O I/H I ratio is identical for all components. The same assumption is applied in Noterdaeme et al. (2012). It is unclear whether this assumption is appropriate for a high-precision measurement and we leave out these two measurements from further comparisons.

A new sample of very precise deuterium abundance measurements (≈ 4 per cent uncertainties) was presented by Cooke et al. (2014). They selected absorbers using narrow selection criteria to allow both precise and robust measurements; for example, they restricted the column density range to damped and sub-damped Lyman α systems, i.e. $\log(N\text{H I})) \geq 19$. The obtained precision demonstrated the future prospects for deuterium as a cosmological probe. However, several important potential systematic errors remain, including the difficulties of modelling the uncertain velocity structure of individual absorbers, and estimating the uncertainties relating to continuum placement.

It is therefore necessary to obtain a significant sample of deuterium measurements so that it becomes possible to detect any plateau in D/H versus redshift or metallicity in order to obtain the primordial value, rather than relying on a small number of measurements where any intrinsic scatter cannot be reliably detected.

At $z = 3.572$, our new measurement has the highest redshift in the sample and one of the lowest column densities. The precision we obtain is comparable to those of Cooke et al. (2014) despite the new system being more complicated and lower column density. This demonstrates the future possibilities for a sample of high-resolution measurements as low column density absorbers are a lot more common than high column density absorbers. The last decade has seen a massive increase in the number and quality of high-resolution quasar spectra that have not yet been systematically searched for suitable low column density absorbers with visible deuterium lines.

The weighted and unweighted averages centre on very nearby values of $(D/H)_p = 2.53 \pm 0.17$ and $(D/H)_p = 2.55 \pm 0.03$, respectively, which can be compared with the recent prediction from standard BBN of $(D/H)_p = 2.45 \pm 0.05$ (Coc et al. 2015; Planck Collaboration III 2016). The deviation between the weighted average and Planck value is $(2.55 - 2.45)/\sqrt{0.03^2 + 0.05^2} = 1.7\sigma$; that is, there is no significant difference. However, the offset in the central values may indicate that some systematic error still remains despite the increasing data quality.

Fig. 4 does not reveal any strong correlations between D/H and redshift, metallicity or column density, but some scatter remains. According to recent chemical evolution modelling, we should expect some internal scatter in D/H measurements arising purely from the difference in the merger and star formation history of individual haloes (Dvorkin et al. 2016). Further high-quality measurements are

needed to establish whether the different halo histories can explain the remaining scatter.

The most outlying D/H values in the sample are also the measurements with the highest uncertainties. If we define a high-precision sample by requiring $(\delta_{\mathrm{D/H}})/(\mathrm{D/H}) < 0.15$, we automatically exclude the four most outlying points in Fig. 4 and the weighted average become $(\mathrm{D/H})_{\mathrm{p}} = 2.56 \pm 0.03$ consistent with the full sample value of 2.55 ± 0.03.

4.4 The baryon fraction

Assuming that the total deuterium-to-hydrogen ratio is reflected by D I/H I, we can derive the primordial value $(\mathrm{D/H})_{\mathrm{p}}$ because there are no sources of astrophysical production (Epstein, Lattimer & Schramm 1976; Prodanović & Fields 2003) and the destruction rate in stars is low at the relevant redshifts and metallicities (Romano et al. 2006; Dvorkin et al. 2016).

$\Omega_b h^2$ can be obtained using fitting relations for standard BBN calculations (e.g. Simha & Steigman 2008; Steigman 2007, 2012; Coc et al. 2015). The most recent update with particular focus on the nuclear reactions gives (Coc et al. 2015)

$$10^5(\mathrm{D/H}) = (2.45 \pm 0.04)\left(\frac{\Omega_b h^2}{0.022\,25}\right)^{-1.657}, \qquad (1)$$

where the uncertainty of 0.04 reflects the measured uncertainties in the nuclear reaction rates. The results from the existing D/H measurements and the averaged values are listed in Table 4. Several of the measurements in the table have percentage level statistical uncertainty, which is comparable to the uncertainty on the nuclear reaction rates. However, most of the quoted uncertainties do not take systematic uncertainties into account. In particular, the uncertainties related to the number of modelled components and the risk of hydrogen blends at the position of deuterium requires high-resolution, high-quality spectra and are best controlled by having a large sample of high-precision measurements.

4.5 Dipole fit

Variations in fundamental constants such as the fine structure constant, the hadronic masses or binding energies would lead to variations in the light element abundances (Dmitriev, Flambaum & Webb 2004; Dent, Stern & Wetterich 2007; Flambaum & Wiringa 2007; Berengut, Flambaum & Dmitriev 2010). Berengut et al. (2011) investigated whether the observed scatter in the D/H measurements could be due to a dipole similar to the one observed for the fine structure constant (Webb et al. 2011; King et al. 2012). Although the significance of the fine structure constant dipole may be somewhat reduced by instrumental effects (Whitmore & Murphy 2015), here we investigate whether a dipole in the same direction is preferred by the deuterium measurements and we also consider the dipole direction as a free parameter. The dipole is described by

$$\log(N(D)/N(H)) = m_{\mathrm{D}} + d_{\mathrm{D}} r \cos(\psi(\phi_d, \theta_d)), \qquad (2)$$

where m_{D} is the average observed deuterium abundance (the monopole), d_{D} is the magnitude of the dipole, $r = ct$ is the look-back distance and $\psi(\phi_d, \theta_d)$ is the angle between a given observation with (RA, Dec.) = (ϕ, θ) and the dipole direction (ϕ_d, θ_d) given by

$$\cos \psi = \cos(\phi - \phi_d)\cos(\theta)\cos(\theta_d) + \sin(\theta)\sin(\theta_d). \qquad (3)$$

The best fits with and without fixing the direction of the dipole are shown in Fig. 5 and the parameters given in Table 5 . The preferred slopes are close to zero with uncertainties larger than the preferred
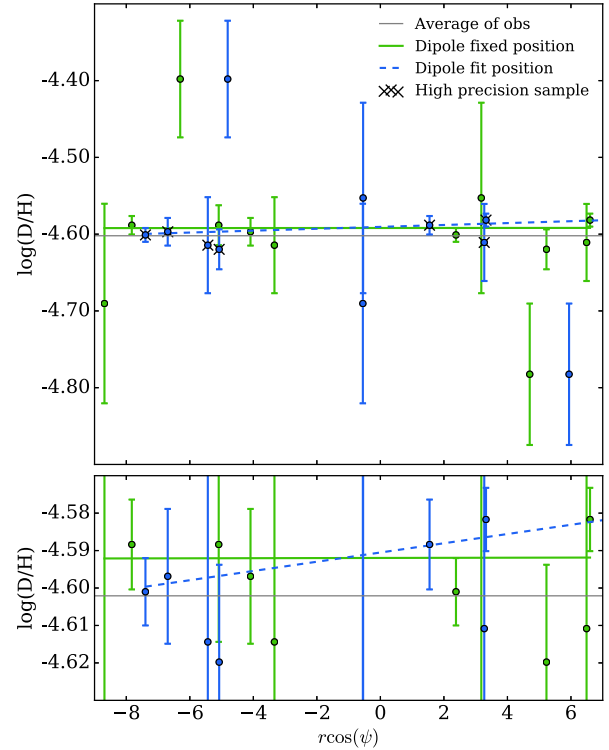
Figure 5. The best fit to the dipole model of Berengut et al. (2011) for fixed position (thick green line) and varying position (dashed blue line) as well as the observed abundances relative to the dipole directions (green and blue data points) and the average of the deuterium measurements (the monopole, thin grey line). The lower panel is a zoom of the *y*-axis. The crosses mark the high precision sample defined by less than 15 per cent uncertainty on D/H. The fits to the high-precision sample (not shown) lies very close to the full sample fits. The parameters are given in Table 5.

Table 5. Best-fitting parameters for fitting the variation in the deuterium measurements with the dipole model in equation (2).

	Full sample		High precision sample	
	Fixed position	Fit position	Fixed position	Fit position
m_{D}	−4.592(6)	−4.59(1)	−4.592(4)	4.590(6)
d_{D}	0.000 002(114)	0.0012(14)	0.000 25(75)	0.0014(6)
RA (h)	17.4 ± 1.0	24.0 ± 5.3	17.4 ± 1.0	0 ± 2
Dec. (°)	-61 ± 10	29.5 ± 70.7	-61 ± 10	21.5 ± 32
χ^2	15.55	13.80	4.01	1.50
χ^2/dof	1.56	1.72	0.67	0.38
$\Delta\mathrm{BIC}^a$	–	–	2.1	2.1
Evidence^b	–	–	Positive	Positive

Notes. ^{a}Difference in Bayesian Information Criterion $\Delta\mathrm{BIC} = \mathrm{BIC}_{\mathrm{slope}} - \mathrm{BIC}_{\mathrm{no\,slope}}$.
^{b}Evidence for preference of a zero slope model (no dipole) relative to a model with dipole based on the Bayesian Information Criterion.

value and consequently consistent both with a small dipole and with no dipole. Despite the increase in sample size and precision, the scatter does not allow us to draw any firm conclusions about anisotropy.

We also fit to the high-precision sample defined by less than 15 per cent uncertainty on D/H (Section 4.4). For fixed position, this is consistent with no dipole. When fitting the high-precision sample for the position, a dipole is preferred with around 2σ significance, but with a very large uncertainty on the direction and a $\chi^2 \ll 1$ indicating too many free parameters in the fit.

4.6 Inhomogeneities

An interesting aspect of D I/H I is that deuterium was produced when the universe was 100 sec old and the temperature around 10^9 K. At that time the horizon size was $2ct = 6 \times 10^{12}$ cm. By today, this causally connected region has expanded by a factor of about $10^9/3$ and so spans 2×10^{21} cm or ~1 kpc. Regions larger than this (or collapsing down from regions larger than this) will have been causally disjoint at the time of deuterium synthesis. This implies that a sufficiently large sample of deuterium measurements will allow us to measure the homogeneity of the universe.

4.7 Dark matter constraints

Primordial element abundances may be very sensitive to the presence of the low-mass dark matter (Steigman 2012; Bœhm et al. 2013; Nollett & Steigman 2014; Archidiacono et al. 2015; Stadnik & Flambaum 2015). For example, in scenarios where a scalar dark matter field interacts with the standard model fields during nucleosynthesis spatial variation in the D I/H I ratio may arise (Stadnik & Flambaum 2015). Using the dipole constraints from Section 4.5, we can improve the constraint on the product of the fractional energy density's spatial gradient with the interaction strength by a factor of roughly 40 relative to Stadnik & Flambaum (2015) as a consequence of the improved dipole constraint. The comparison of the calculated and measured deuterium abundances should lead to another breakthrough in the precision (Berengut, Stadnik & Flambaum, private communication).

5 CONCLUSIONS

From the analysis of the $z_{abs} = 3.572$ absorption system in high-quality Keck and VLT spectra of quasar PKS1937–101, we make the following conclusions:

(i) We find the D I/H I ratio in this absorber to be $2.62 \pm 0.05 \times 10^{-5}$ that corresponds to $100\Omega_b h^2 = 2.14 \pm 0.03$ for standard BBN. This value deviates by 1.7σ from the *Planck* measurement of $100\Omega_b h^2 = 2.225 \pm 0.016$ and is considered consistent.

(ii) Independent fits to this absorption system using Keck and VLT spectra give consistent results.

(iii) The analysis presented here shows that lower column density systems can provide a precision on D I/H I comparable to higher column density DLAs (Cooke et al. 2014). This is important because the neutral hydrogen column density distribution in quasar absorption systems is a steep power law, with lower column density systems being more common. A statistically large sample of measurements is therefore feasible and necessary to reveal a plateau of primordial values as a function of, e.g. metallicity.

(iv) The spatial variation of the observed high-precision deuterium abundances is consistent with no dipole.

Deuterium abundance measurements using quasar absorption systems offer rare tests of the standard model of BBN and models with non-standard physics. While CMB measurements do offer high-precision measurements of the baryon density, a model of BBN must be assumed. However, beyond-standard models involving, for example, additional relativistic particle species or dark matter particles, often imply different conditions in the two epochs that can lead to different D I/H I expectation values (Steigman 2013). Therefore, studying both epochs observationally and comparing the independent constraints on the baryon density is an important opportunity to discover or rule out physics beyond the standard model.

REFERENCES

Archidiacono M., Hannestad S., Hansen R. S., Tram T., 2015, Phys. Rev. D, 91, 065021

Aver E., Olive K. A., Skillman E. D., 2015, J. Cosmol. Astropart. Phys., 7, 011

Bahcall J., Wolfe R., 1968, ApJ, 152

Balashev S. A., Zavarygin E. O., Ivanchik A. V., Telikova K. N., Varshalovich D. A., 2016, MNRAS, 458, 2188

Berengut J., Flambaum V., Dmitriev V., 2010, Phys. Lett. B, 683, 114

Berengut J. C., Flambaum V. V., King J. A., Curran S. J., Webb J. K., 2011, Phys. Rev. D, 83, 123506

Burles S., Tytler D., 1997, AJ, 114, 1330

Burles S., Tytler D., 1998a, ApJ, 499, 699

Burles S., Tytler D., 1998b, ApJ, 507, 732

Bœhm C., Dolan M. J., McCabe C., 2013, J. Cosmol. Astropart. Phys., 8, 41

Coc A., Petitjean P., Uzan J.-P., Vangioni E., Descouvemont P., Iliadis C., Longland R., 2015, Phys. Rev. D, 92, 123526

Cooke R. J., Pettini M., Jorgenson R. A., Murphy M. T., Steidel C. C., 2014, ApJ, 781, 31

Crighton N. H. M., Webb J. K., Ortiz-Gil A., Fernández-Soto A., 2004, MNRAS, 355, 1042

Dent T., Stern S., Wetterich C., 2007, Phys. Rev. D, 76, 063513

Di Valentino E., Melchiorri A., Mena O., 2013, J. Cosmol. Astropart. Phys., 11, 18

Dmitriev V. F., Flambaum V. V., Webb J. K., 2004, Phys. Rev. D, 69, 063506

Dvorkin I., Vangioni E., Silk J., Petitjean P., Olive K. A., 2016, MNRAS, 458, L104

Epstein R. I., Lattimer J. M., Schramm D. N., 1976, Nature, 263, 198

Ferland G. J. et al., 2013, Rev. Mex. Astron. Astrofis., 49, 137

Fields B. D., Olive K. A., Silk J., Cassé M., Vangioni-Flam E., 2001, ApJ, 563, 653

Fixsen D. J., 2009, ApJ, 707, 916

Flambaum V. V., Wiringa R. B., 2007, Phys. Rev. C, 76, 054002

Fox A. J., Ledoux C., Petitjean P., Srianand R., 2007, A&A, 473, 791

Fumagalli M., O'Meara J. M., Prochaska J. X., 2011, Science, 334, 1245

Izotov Y. I., Thuan T. X., Guseva N. G., 2014, MNRAS, 445, 778

Kim T.-S., Partl A. M., Carswell R. F., Müller V., 2013, A&A, 552, A77

King J. A., Webb J. K., Murphy M. T., Flambaum V. V., Carswell R. F., Bainbridge M. B., Wilczynska M. R., Koch F. E., 2012, MNRAS, 422, 3370

Kirkman D., Tytler D., Suzuki N., O'Meara J. M., Lubin D., 2003, ApJS, 149, 1

Lanzetta K. M., Wolfe A. M., Turnshek D. A., Lu L., McMahon R. G., Hazard C., 1991, ApJ, 77, 1

Nollett K. M., Steigman G., 2014, Phys. Rev. D, 89, 083508

Noterdaeme P., López S., Dumont V., Ledoux C., Molaro P., Petitjean P., 2012, A&A, 542, L33

O'Meara J. M., Tytler D., Kirkman D., Suzuki N., Prochaska J. X., Lubin D., Wolfe A. M., 2001, ApJ, 552, 718

O'Meara J. M., Burles S., Prochaska J. X., Prochter G. E., Bernstein R. A., Burgess K. M., 2006, ApJ, 649, L61

Penton S. V., Stocke J. T., Shull J. M., 2004, ApJS, 152, 29

Pettini M., Bowen D. V., 2001, ApJ, 560, 41

Pettini M., Cooke R., 2012, MNRAS, 425, 2477

Pettini M., Zych B. J., Murphy M. T., Lewis A., Steidel C. C., 2008, MNRAS, 391, 1499

Planck Collaboration XIII, 2016, A&A, 594, A13

Prodanović T., Fields B. D., 2003, ApJ, 597, 48

Riemer-Sørensen S. et al., 2015, MNRAS, 447, 2925

Romano D., Tosi M., Chiappini C., Matteucci F., 2006, MNRAS, 369, 295

Simha V., Steigman G., 2008, J. Cosmol. Astropart. Phys., 6, 16

Songaila A., Wampler E. J., Cowie L. L., 1997, Nature, 385, 137

Stadnik Y. V., Flambaum V. V., 2015, Phys. Rev. Lett., 115, 201301

Steigman G., 2007, Ann. Rev. Nucl. Part. Sci., 57, 463

Steigman G., 2012, preprint (arXiv:1208.0032)

Steigman G., 2013, Phys. Rev. D, 87, 103517

Tytler D., Fan X.-M., Burles S., 1996, Nature, 381, 207

Wampler E. J., 1996, Nature, 383, 308

Webb J. K., King J. A., Murphy M. T., Flambaum V. V., Carswell R. F., Bainbridge M. B., 2011, Phys. Rev. Lett., 107, 191101

Whitmore J. B., Murphy M. T., 2015, MNRAS, 447, 446

Wolfe A. M., Prochaska J. X., 2000, ApJ, 545, 591

SUPPORTING INFORMATION

Supplementary data are available at *MNRAS* online.

j1939v6.2_redtable.tex

Please note: Oxford University Press is not responsible for the content or functionality of any supporting materials supplied by the authors. Any queries (other than missing material) should be directed to the corresponding author for the article.

APPENDIX A: MODEL

Table A1. The best-fitting parameter values for the four component model.

Component	Redshift	Species	$\log(N)$[a]	b_{turb} or b_{tot} (km s^{-1})	$T\,(10^4\,\mathrm{K})$
A	$3.572\,135 \pm 0.000\,007$	H I	17.575	2.36 ± 1.43	1.64 ± 0.03
		D I	12.994	2.36 ± 1.43	1.64 ± 0.03
		C II	12.360	2.36 ± 1.43	1.64 ± 0.03
		Si II	11.197	2.36 ± 1.43	1.64 ± 0.03
		Fe III	12.502	2.36 ± 1.43	1.64 ± 0.03
		Si IV	11.699	2.36 ± 1.43	1.64 ± 0.03
B	$3.572\,268 \pm 0.000\,002$	H I	17.311	2.15 ± 0.76	1.81 ± 0.42
		D I	12.730	2.15 ± 0.76	1.81 ± 0.42
		C II	12.777	2.15 ± 0.76	1.81 ± 0.42
		Si II	12.031	2.15 ± 0.76	1.81 ± 0.42
		Fe III	12.810	2.15 ± 0.76	1.81 ± 0.42
		Si IV	12.678	2.15 ± 0.76	1.81 ± 0.42
C	$3.572\,451 \pm 0.000\,002$	H I	17.402	4.51 ± 0.23	1.87 ± 0.07
		D I	12.821	4.51 ± 0.23	1.87 ± 0.07
		C II	13.160	4.51 ± 0.23	1.87 ± 0.07
		Si II	12.311	4.51 ± 0.23	1.87 ± 0.07
		Fe III	13.220	4.51 ± 0.23	1.87 ± 0.07
		Si IV	12.822	4.51 ± 0.23	1.87 ± 0.07
D	$3.572\,682 \pm 0.000\,020$	H I	15.943	1.58 ± 8.66	4.35 ± 0.94
		D I	11.362	1.58 ± 8.66	4.35 ± 0.94
		Si II	11.242	1.58 ± 8.66	4.35 ± 0.94
		Si IV	11.082	1.58 ± 8.66	4.35 ± 0.94
Summed		Species	$\sum \log(N)$		
		H I	17.925 ± 0.006		
		D I	13.345 ± 0.006		
		C II	13.357 ± 0.029		
		Si II	13.345 ± 0.006		
		Fe III	13.419 ± 0.029		
		Si IV	13.080 ± 0.005		
		O I	12.060 ± 0.127[b]		
Velocity shift		Data[c]	Shift (km s^{-1})		
		setup 2	–		
		setup 3	-1.326 ± 0.089		
		setup 5	0.714 ± 0.066		
		setup 10	-0.491 ± 0.064		
		VLT	0.504 ± 0.061		
		VLT Lyman 5	1.122 ± 0.138		

Table A1 – *continued.*

Blends	Redshift	Species	log (N)	b (km s^{-1})
Si II 1193 Å	3.487 11	H I	13.048	36.93
	3.487 89	H I	12.073	9.77
Si II 1304 Å	3.411 50	H I	13.062	21.61
Fe III 1122 Å	3.221 10	H I	14.952	21.04
	3.222 83	H I	12.096	22.28
	3.223 76	H I	14.191	20.91
Si IV 1393 Å	4.242 75	unknown	12.214	17.29
H I 1216 Å (Lyman α)	3.580 17	H I	12.372	13.77
	3.579 73	H I	12.571	30.64
	3.578 47	H I	13.661	21.94
	3.577 75	H I	13.476	17.68
	3.577 33	H I	12.935	^{d}21.91
	3.576 68	H I	13.644	20.45
	3.575 60	H I	12.827	29.26
	3.575 03	H I	12.270	15.70
	3.574 62	H I	12.372	^{d}29.61
	3.573 36	H I	13.465	6.89
	3.573 08	H I	14.999	^{d}29.58
	3.569 51	H I	13.085	34.30
	3.569 35	H I	11.473	8.32
	3.568 25	H I	12.331	27.72
	3.567 15	H I	13.450	31.23
	3.566 39	H I	14.084	29.03
	3.564 97	H I	14.131	27.00
	3.564 71	H I	14.029	40.28
H I Å (Lyman γ)	2.656 62	H I	11.920	8.50
	2.656 13	H I	13.487	26.67
	2.656 93	H I	12.459	14.64
	2.659 21	H I	12.526	8.41
	2.659 74	H I	14.345	37.06
	2.660 65	H I	12.686	^{d}20.00
	2.661 01	H I	12.841	9.13
	2.661 39	H I	12.579	12.88
H I Å (Lyman 4)	2.569 77	H I	13.442	27.41
	2.571 24	H I	13.847	23.74
	2.573 07	H I	13.026	^{d}20.00
	2.573 78	H I	14.632	30.51
	2.574 49	H I	13.727	23.11
H I Å (Lyman 5)	2.524 87	H I	13.374	26.72
	2.525 28	H I	13.154	22.48
	2.525 77	H I	12.834	12.51
	2.526 09	H I	12.916	20.95
	2.527 94	H I	12.845	^{d}20.21
H I Å (Lyman 6)	2.499 14	H I	13.443	58.82
	2.499 45	H I	13.548	23.38
	2.500 11	H I	11.793	1.31
	2.502 24	H I	13.156	26.30
	2.502 69	H I	12.542	17.98
H I Å (Lyman 7)	2.481 72	H I	11.550	1.00
	2.482 19	H I	12.755	27.04
	2.483 05	H I	12.312	12.89
	2.484 32	H I	13.050	^{d}20.00
	2.485 12	H I	14.446	31.57
H I Å (Lyman 8)	2.469 46	H I	13.255	26.35
	2.471 50	H I	13.541	20.62
	2.471 01	H I	13.213	31.34
	2.472 92	H I	13.177	31.21
	2.474 37	H I	13.019	^{d}40.65
	2.474 92	H I	13.812	30.13
	2.475 34	H I	13.489	19.67

Table A1 – *continued.*

Blends	Redshift	Species	log (*N*)	*b* (km s⁻¹)
H I Å (Lyman 9)	2.462 14	H I	12.992	39.16
	2.462 65	H I	12.744	16.01
	2.463 17	H I	14.130	29.01

Notes. ᵃFor the summed column densities, the individual uncertainties are not determined.
ᵇBased on a constant ratio of O I/H I across all components.
ᶜsetup 2, setup 3, setup 5 and setup 10 corresponds to the four different stacks of the Keck observations in Table 1, while all the VLT exposures are combined into one spectrum.
ᵈA few of the *b*-parameters were fixed to prevent them from getting unphysically large.

This paper has been typeset from a TEX/LATEX file prepared by the author.